Operando Auger/XPS using an electron beam to reveal the dynamics/morphology of Li plating and interphase formation in solid-state batteries

Julien Morey, Jean-Bernard Ledeuil, Hervé Martinez, Lénaïc Madec

ARTICLE

Operando Auger/XPS using electrons beam to reveal the dynamics/morphology of Li plating and interphase formation in solid-state batteries

Received 00th January 20xx,
Accepted 00th January 20xx

DOI: 10.1039/x0xx00000x

Julien Morey,*[a] Jean-Bernard Ledeuil[a], Hervé Martinez [abc] and Lénaïc Madec [*ab]

Interfaces and their understanding/control are the key to pave the way for the development of solid-state batteries. This work focuses on the development of *operando* Auger cycling using electrons beam to investigate the Li/solid electrolyte (SE) interphases. To do so, the fully tunable electron gun of the Auger was applied on top of a model Li/Li_6PS_5Cl(Arg) stack, allowing the charge built up at the Arg surface and Li^+ migration from the lithium electrode followed by SE interphase formation and Li plating. Overall, it is found that (i) Li_6PS_5Cl is first reduced into Li_2S, LiCl and Li_3P while (ii) Li platting occurs almost concomitantly and (iii) proceeds until the end of the *operando* cycling. These results were then confirmed by *operando* XPS using electrons beam. Importantly, this study highlights that *operando* Auger is more powerful than *operando* XPS as it provides visual observation of the dynamics/morphology of both Li/solid electrolyte interphase formation and Li plating together with reliable chemical information. This study thus open the door for future development of *operando* Auger cycling using electrons beam as a powerful approach to better understand the interfaces in solid-state batteries.

Introduction

Lithium-ion batteries play a key role in today's society. Indeed, they are used to power portable electronic devices, tools and electric/hybrid-electric vehicles as well as for grid storage of renewable wind/solar energies. However, further improvements in term of energy and/or power densities together with a longer lifetime and improved safety at an affordable cost, are mandatory to meet future requirements[1], especially for electric vehicles. In that direction, all-solid-state batteries (ASSBs) offer a promising solution[2,3] as they could increase the volumetric energy density up to 50 % and the gravimetric energy density up to 150 % compared with conventional liquid electrolyte-based Li-ion batteries. ASSBs are based on solid electrolytes (SE), which are composed of quasi non-flammable materials such as ceramics, polymers or a combination of them and act as both the ion conduction medium and the separator. The expected energy density increase originates from (i) the use of metallic lithium at the anode, (ii) the increase of the electrochemical voltage stability window and (iii) the more flexible/compact cell packaging. Nevertheless, numerous challenges need to be solved in order to develop a new market based on this technology.

[a.] *Université de Pau et des Pays de l'Adour, E2S UPPA, CNRS, IPREM, Pau, France. E-mail : julien.morey@univ-pau.fr; lenaic.madec@univ-pau.fr*
[b.] *Réseau sur le Stockage Electrochimique de l'Energie, CNRS FR3459, Amiens, France.*
[c.] *Centrale Casablanca, Centre de Recherche Systèmes Complexes et Interactions, Ville Verte Bouskoura, Maroc.*

First, the ionic conductivity of solid electrolytes (SE) still remains relatively low, especially for polymer based SE. More importantly, the electro-chemo-mechanical stability of the numerous solid electrode materials/SE interfaces is still unsatisfactory[4,5]. SE materials are also difficult to process[6], especially for ceramic solid-state batteries, for which it is difficult to achieve good Li ion transport between ceramics and electrode materials[7]. Second, at the anode, the best possible material is Li metal, but its use remains limited by possible dendrite formation and SE degradation at its surface, which can lead to rapid rollover of the cell[8–10]. Beyond the choice of SE and electrode materials, true battery performance in terms of cycle and calendar life, such as voltage window/profile and impedance are often lower/worse than expected due to parasitic reactions at the electrode materials/SE interfaces. The origin of these decomposition reactions is thermodynamic. More specifically, if the chemical potentials μ_A (anode) and μ_C (cathode) are within the SE electrochemical stability window, the active materials/SE interfaces are stable.[11] However, this ideal case almost never happens so that solid electrolyte interphases (SEI) are formed, similarly to liquid Li-ion batteries. In ASSBs, SEI can originated from cell storage/cycling as well as from the sequential manufacturing processes, especially for ceramic based SE[6]. The ideal SEI should, however, meet several requirements such as high ionic conductivity, compact structure and sufficient mechanical properties (both high elastic and shear strength) to suppress lithium dendrites formation. In practice, SEI are often unstable and/or inhomogeneous and become thicker over time, which increases the electrode materials/SE resistance and thus decrease the electrochemical performance. Therefore, in ASSBs, it is better to limit the mixing

of components and stack preparation steps to hinder the formation of electrode materials/SE interphases and thus preserve the intrinsic properties of each material. Despite the numerous materials combination proposed for ASSBs in the literature, the electrode materials/SE interfaces studies remains very sparse compared to the hundreds of papers reported in liquid Li-ion batteries. This is explained by the challenge to reveal and analyse the interfacial regions with high reliability as they are buried in the entire ASSB stacks.

In that direction, state-of-the-art cross-section preparation techniques such as focused ion beam (FIB) or broad ion beam (BIB) are often necessary before analytical techniques can be used to characterize the buried interfaces. In that case, *ex situ* cycling is used as the most common method and consists in electrochemically cycling the ASSB cell, disassembled it, then reveal the buried interfaces prior to the analysis using so far: optical microscopy (OM)[12–17], scanning electron microscopy (SEM),[18–20] high-resolution transmission electron microscopy (HR-TEM)[18,21–23] combined with chemical/structural analyses by electron energy loss spectroscopy (EELS)[18] or energy dispersive spectroscopy (EDS)[24–26], scanning electron microscopy (SEM)[26–30], Raman spectroscopy[31], Time of flight secondary ion mass spectrometry (ToF-SIMS)[32–35], Auger electron spectroscopy[25] and X-ray Photoelectron Spectroscopy (XPS)[24,36–42] Electrochemical impedance spectroscopy (EIS) has also been extensively used to investigate electrochemical interfacial changes[43–45] but careful precaution should be taken as this technique examines all interfaces of the ASSB stacks and does not necessarily make distinction among the different interfaces. Furthermore, *in situ* and *operando* approaches are very attractive as they allow analysing ''in real time'' and limit possible sample pollution/interfaces degradation induced by the cell disassembling and sample preparation. During *in situ*, the ASSB cell is sequentially cycled and analysed inside an analysis chamber. During *operando*, the cell is cycled at the same time the analysis is performed. For *in situ* cycling, dedicated cells need to be design to fit in the analytical machine used. For *operando* cycling, the dynamic evolution of the electrode materials and electrode materials/SE interfaces can be directly followed with minimal sample preparation and concomitant possible alteration. Note that considering the numerous *in situ*/*operando* cells setup reported so far, it is difficult to discuss about their respective advantage and limitation. Therefore, the standardization of the cells setups and also of the experimental setups will need to be address in the future in order to get more reliable and reproducible experiments between laboratories. While different *operando* cycling cells are described in the literature,[46] the major interest of *operando* is that it can be performed without any specific dedicated cell. Indeed, the electron and/or UV sources can be used instead to discharge/charge the ASSBs stack[47–49]. Typically, the charge compensation gun present in XPS and ToF-SIMS apparatus is used in electron flooding mode while the primary electron beam is used for SEM/Auger analysis. Moreover, the UV source, often present in XPS equipment can be used to reversibly cycle the ASSB stack by removing valence band electrons. This *operando* approach thus suppresses the need for cross-section preparation as well as the need to adapt the ASSB stack to the format/dimension of the electrochemical cell and so on. In that case, the main drawback remains the lack of pressure control on the ASSB stack, which can be critical only if high current are used, especially for ceramic SE. Indeed, the most common use and interest of this approach so far, is to study the Li/SE interfaces formation that cannot be access by *ex situ* or *in situ* cycling/analysis.[50–52] Note that to our knowledge, this *operando* approach using an electron gun has been proposed two times for XPS[47,49], only one time for Auger[49] and remains to be developed for ToF-SIMS. Moreover, the previous *operando* Auger study only reported elemental mapping evolution without chemical/spectral information while such data are of high interest and are even essential to get a reliable understanding.

To fill this gap, the present work focuses on the use of *operando* Auger cycling using electrons beam to illustrate the high interest of this approach with a comparison with *operando* XPS also using electrons beam. To do so, the electrochemical stability of a model $Li_{(M)}/Li_6PS_5Cl$ system is investigated during Li plating. Note that Li_6PS_5Cl is well known to be reduced as follow[24,56,58]: $Li_6PS_5Cl + 8\ Li^+ + 8\ e^- \rightarrow LiCl + Li_3P + 5\ Li_2S$. Li_6PS_5Cl is thus used here to validate the *operando* Auger approach and to make a reliable comparison with *operando* XPS. It is showed that *operando* Auger allows mapping and analysing the dynamic Li/SE interfaces formation with chemical environment as well as visualizing the Li plating at both micro- and nano-scales. *Operando* XPS shows similar chemical environment evolution but at the micro-scale and with no optical information. Overall, this work opens the door for future developments of *operando* Auger cycling using electrons beam and paves the way for a better understanding of interphases formation in ASSBs.

Materials and methods

Li_6PS_5Cl (99.9%, Ampcera, noted Arg thereafter) was used as received. Inside an Ar filled-glovebox (H_20 <0.1 ppm and O_2 <0.1 ppm), pellets of 10 mm diameter were made by pressing 120 mg of Arg under 375 MPa (3T) during 5 min, which led to about 600 µm thick pellets. The Arg pellets were placed on top of a lithium foil (GoodFellow, 99.9 %, thickness of 0.2 mm) then deposited on an Auger/XPS sample holder. For comparison, Arg pellets were also used without Li (as reference) to evaluate any possible damage induced by the electron beam in Auger and XPS. The Li/Arg stacks or Arg pellets were transferred into the machines using a transfer vessel (Auger) or an Ar filled-glovebox directly connected (XPS) to prevent any air contamination. Once inside the Auger/XPS analysis chambers, sample holders are being grounded so that the electron flow applied on top of the Li/Arg stacks will create a potential difference by charges build up, which will then induce Li^+ migration from the lithium electrode, SEI formation if any then Li plating (Fig. 1).

Operando SEM/Auger cycling using electrons beam was performed using a JEOL JAMP95000F working under ultra-high vacuum (1.5×10^{-9} mbar) during analysis. Typically, the sample was tilt to 45° (an optimal angle in such operating conditions) to prevent any possible charging effect. The electrons beam was

fixed at 5.10^{-8} A and 10 KeV, corresponding to a cycling rate of about 0.8 $mA.cm^{-2}$. *Operando* SEM/Auger cycling using electrons beam was performed by alternatively recording (60 times) a SEM image (magnification of about x800, duration <10 s) and an Auger survey spectrum (large area scan of 30 x 20 µm, *i.e.* average spectrum obtained from 256 x 256 points, with dE/E = constant = 0.5 %, kinetic energy from 20 to 600 eV, duration 30 s). Thus, the sample charging is induced by both the Auger/SEM analysis while short time acquisition SEM images (<10 s) are used to follow the morphological evolution.

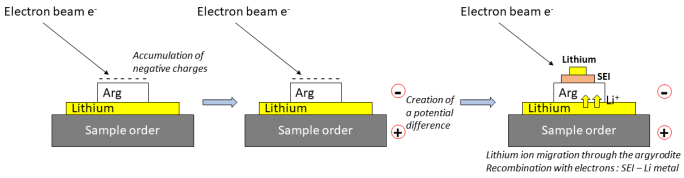

Fig. 1 Schematic view of the operando Auger cycling method used in this work via an electrons beam.

The total duration of the experiment was about 40 min. A "probe tracking" correction was used after each SEM/Survey spectra step to control and compensate any drift. Additionally, for one experiment, scanning Auger microscopy (SAM, elemental 2D distribution) images of Li KVV (from Li_2S and Li metal) and S LVV transitions were also recorded. This acquisition was performed after half of the SEM/Auger spectra steps using the same large area with a 10 eV pass energy and 2 ms dwell time in a fixed energy resolution (dE = constant or constant analyzer energy mode). Duration of the SAM was about 10 min. Images contrast intensity is represented using "peak minus background". Peak fitting processing was performed using the JEOL's peak deconvolution software based on real references spectra.

Operando XPS cycling using electrons beam was performed using a THERMOFISHER ESCALAB 250 Xi with a monochromatized Al Kα radiation (hv= 1486.6 eV) working under ultra-high vacuum (9.0×10^{-9} mbar). *Operando* XPS was performed by recording (12 times) core level spectra every 55 min (elliptic 325 x 650 µm X-ray beam spot, 20 eV pass energy, 0.1 eV step size and short time iterative acquisition scans to follow any possible degradation, duration 5 mins) while using the charge neutralizer (flood gun) in electron mode (in lens only: Beam = 0.1 V, Emission = 100 µA, Focus = 20 V and Extractor = 15 V corresponding to a current applied to the sample of about 3 µA for a surface area of about 0.03 cm^2). The total duration of the experiment was 12 h. Peak fitting was performed using CasaXPS software. The binding energy scale was calibrated from the 285 eV peak of adventitious carbon. A non-linear Shirley-type background was used for core peaks analysis while 70% Gaussian – 30% Lorentzian Voigt peak shapes and full width at half-maximum constraint ranges were selected to optimize areas and peak positions. XPS quantification was performed using the relative sensitivity factor provided from Thermo database (based on modified Scofield cross-sections).

Results and discussion

Operando Auger cycling using electrons beam – Note first that when using only an Arg pellet (*i.e.* without Li foil), no change was observed in SEM images neither in Auger analysis (**Fig. S1**), which highlights that no electron beam damage will occur during the *operando* Auger cycling on the Li/Arg stack. Fig. 2 shows typical SEM images evolution from the beginning to the end of the *operando* cycling procedure. The area where the electron beam is scanned is highlighted by the dotted rectangle. Fig. S2 also provides a short video of the full evolution of the SEM images during the *operando*. Reproducibly was checked by repeating the experiment on another pellet (Fig. S3). At the beginning of the experiment, a slight volume expansion of the Arg surface was first observed with a secondary electron white contrast (Fig. 2b) due to the SEI formation. It is explained by the creation of reduction compounds from the Arg more likely with different density than the Arg. Note that this phenomenon would be an issue in a real cell as it could lead to contact loss at the Li/SE interfaces and thus to possible dendrite formation. Then, the apparition of a thicker layer (~2 to 5 µm) with a secondary electron black contrast was observed (Fig. 2c and d) and is attributed to the Li plating. These results thus suggest that the SEI is first formed followed by Li plating. Regarding the Li plating morphology, it appears relatively rough, *i.e.* it did not take place evenly over the entire surface, leading to an inhomogeneous thickness (see Fig 6 for closer view), which can be attributed to the relatively high current density used for the experiment (about 0.8 $mA.cm^{-2}$). Porous Li may also form under such high current. Note also that measuring precisely the Li thickness over the entire area remains a challenge. In any case, the thickness of the Li expected to be plated at the end of the *operando* Auger is about 2 micron while it appears thicker (up to ~5 micron) in some areas even after only 20 min of experiment (Fig. 2c and d). In addition, the Li plating (black contrast) occurred on a larger area than the scanned one for the experiment (dotted rectangle) more likely due to an electron flow at the Arg surface supported by the well-known electronic conductivity[53] of Arg (~10^{-6} $S.cm^{-1}$ at 25°C from datasheet supplier[54]).

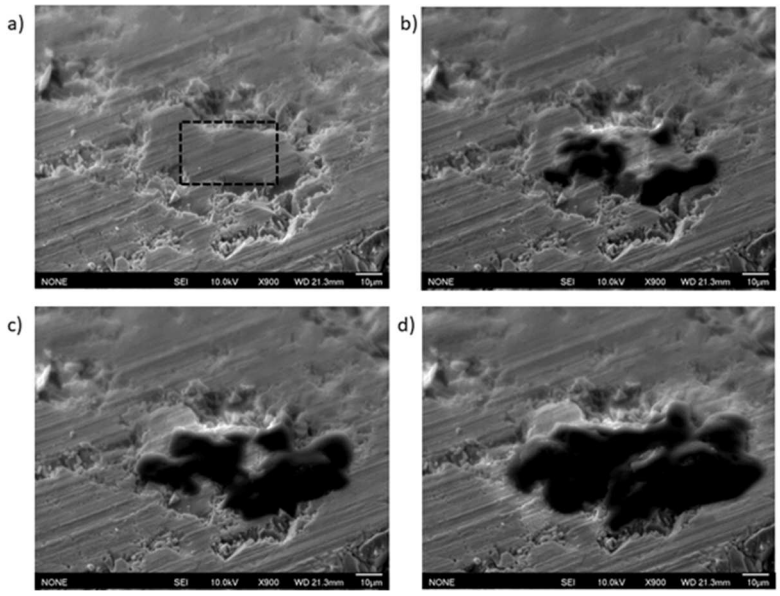

Fig. 2 SEM images of an Arg pellet surface a) before the operando Auger cycling using electrons beam, b) after 10 min, c) 20 min and d) at the end of operando cycling. The dotted rectangle indicates where the operando Auger cycling was performed. Note that the Li expected to be plated is about 0.7 µm, 1.3 µm and 2 µm after 10 min, 20 min and at the end of the *operando* Auger, respectively.

To confirm these hypotheses, Auger spectra and SAM images analysis were then used. Fig. 3 shows the evolution of the Auger spectra recorded as function of the time during the *operando* cycling on a duplicate sample. Auger survey spectra showed the decrease of the P LVV, S LVV and Cl LVV transition peaks from the Arg and the increase of the Li transition peaks (**Fig. 3a**), indicating the covering of the Arg by SEI and/or Li platting. This was confirmed by the evolution of the shape and position of the Li KVV transition that showed the appearance almost simultaneously of Li_2S and Li metal KVV transition peaks after only 2 min (Fig. 3b), according to JEOL references database. This was further confirmed by the fit of the 6 min Li KVV spectrum in derivative representation, (Fig. 3c). These results thus confirm the SEI formation from the Arg reduction during the Li plating, in agreement with the well-known Arg reduction pathway.[55–59] Note that here, the appearance of LiCl should also be observed but it was impossible to confirm it by Auger spectra peak fitting as it would be within the uncertainty of the fitting. It is also possible that the starting Li_6PS_5Cl was already in partial equilibrium with Li_3PS_4 and LiCl so that further reduction would lead only to Li_2S formation

ARTICLE

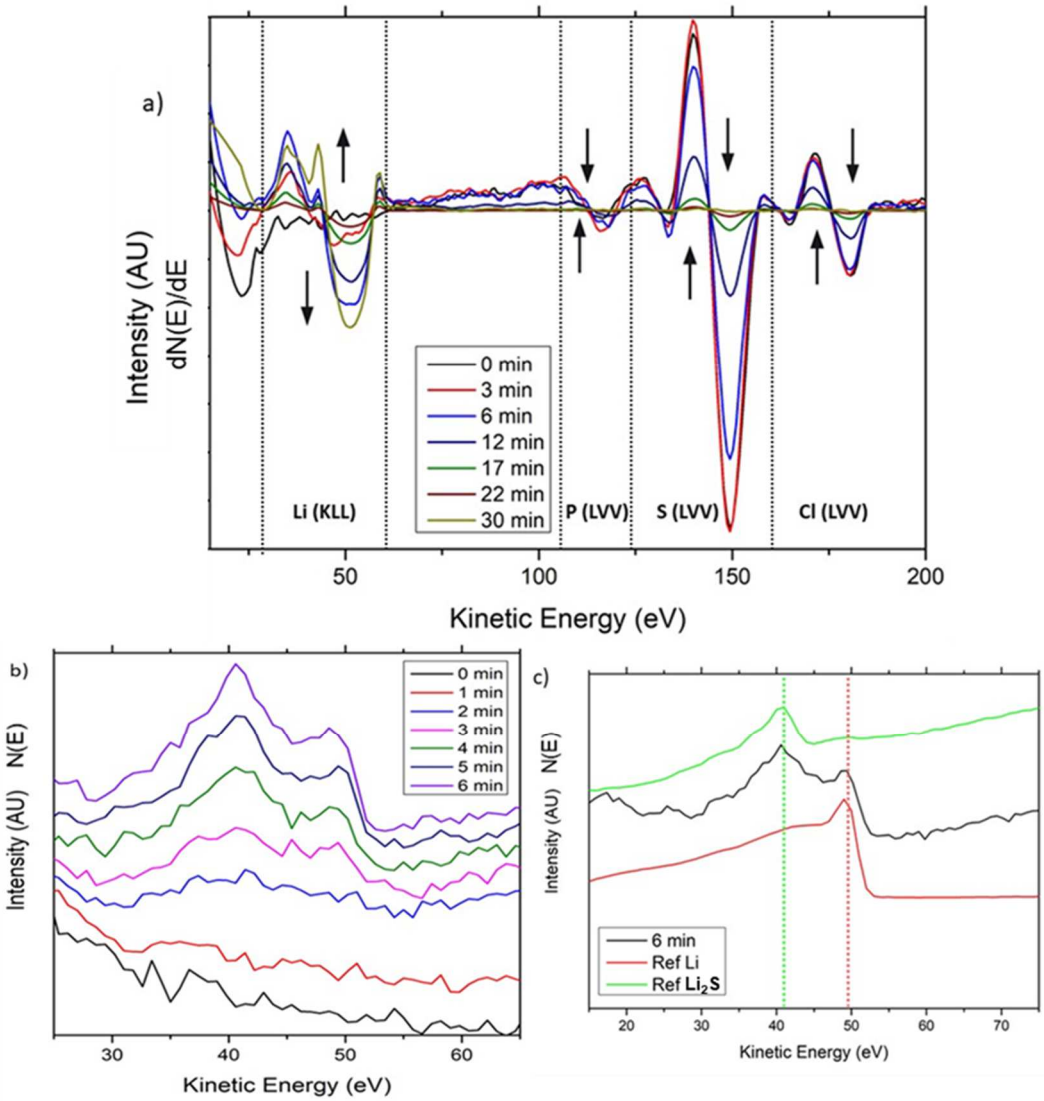

Fig. 3 a) Evolution of the Auger survey spectra in derivate representation as acquired at the Arg pellet surface during the operando Auger cycling using electrons beam, b) zoom on the Li KLL transition of the Auger survey spectra during the beginning of the experiment, c) comparison of the Auger spectrum acquired after 6 min of operando cycling with Auger spectra of Li metal, Li_2S and LiCl from JEOL references as well as the corresponding fitting.

To further visualize the SEI and Li plating formation, additional energy resolved SAM (elemental 2D distribution) images of Li_{metal} KVV, Li_{Li2S} KVV and S LVV transitions were taken in the middle of the SEM/Auger spectra acquisition (see experimental part) as reported in (Fig. 4**)**. The energy resolved SAM image overlay of all transitions clearly shows the Li_2S formation and Li platting. It is also observed that the Li metal covers mostly the Li_2S surface as seen by comparison between the two SAM images. These results further suggest that Li_2S is formed first from the Arg reduction then Li plating occurs.

Operando XPS cycling using electrons beam – In this part, *operando* XPS was performed on a pair sample to confirm the results of the *operando* Auger cycling. Note first that when using

only an Arg pellet (*i.e.* without Li foil), no change was observed in the XPS core level spectra (**Fig. S1**), which highlights that no electron beam damage will occur during the *operando* XPS cycling on the Li/Arg stack. **Figure 5** shows the evolution of the Li 1s, S 2p and O 1s XPS core level spectra recorded as function of the time during the *operando* cycling. **Figure S4** shows the corresponding evolution of the Cl 2p, C 1s and P 2p XPS core level spectra. **Table S1** shows the full XPS quantification (in at.%) while **Table 1** shows the corresponding XPS quantification (in at.%) for the main compounds. Note first that the starting Arg contains about 2 at.% of P_2S_5 and 6.5 at.% of Li_xSO_3 as well as 25.2 at.% of Li_2CO_3, more likely originated from the synthesis (residual P_2S_5) and the storage conditions of the commercial Arg. Overall, these impurities showed a continuous decrease during the *operando* cycling, indicating their covering by new compounds, including the reduction products of the Arg as well as the Li plating. Note also that such relatively high amount of Li_2CO_3 is often observed at Arg surface in the literature while neglected. However, this could increase the contact resistance between Arg and active materials including Li metal and it could thus lead to poorer performance as well as possible Li dendrite formation.

Regarding the evolution of the S 2p doublet of the Arg at about 161.8 eV[39,56], XPS data showed a continuous decrease during the *operando* cycling. Simultaneously, an increase first of the O 1s peak of LiOH (~531.3 eV) then of the O 1s peak of Li_2O (~528.8 eV) were observed. The continuous shift of the Li 1s spectra towards lower binding energy further confirms the LiOH then Li_2O increase. These phenomena are attributed to Li plating with, however, a quick conversion into LiOH then Li_2O, more likely due a reaction of Li with residual oxygen present inside the XPS analysis chamber. This point will be discussed in more details in the following part. In addition, a large increase of Li_2S (about 5 at.%) and a slight increase of LiCl / Li_3P (about 1 at.% both) were observed after 1h, followed by their continuous decrease until the end of the cycling. Overall, these results thus confirm the *operando* Auger cycling: (i) Arg is first reduced following the well-known $Li_6PS_5Cl + 8\ Li^+ + 8\ e^- \rightarrow LiCl + Li_3P + 5\ Li_2S$ reaction pathway; (ii) almost concomitantly, Li plating occur and (iii) then Li plating continues until the end of the *operando* cycling.

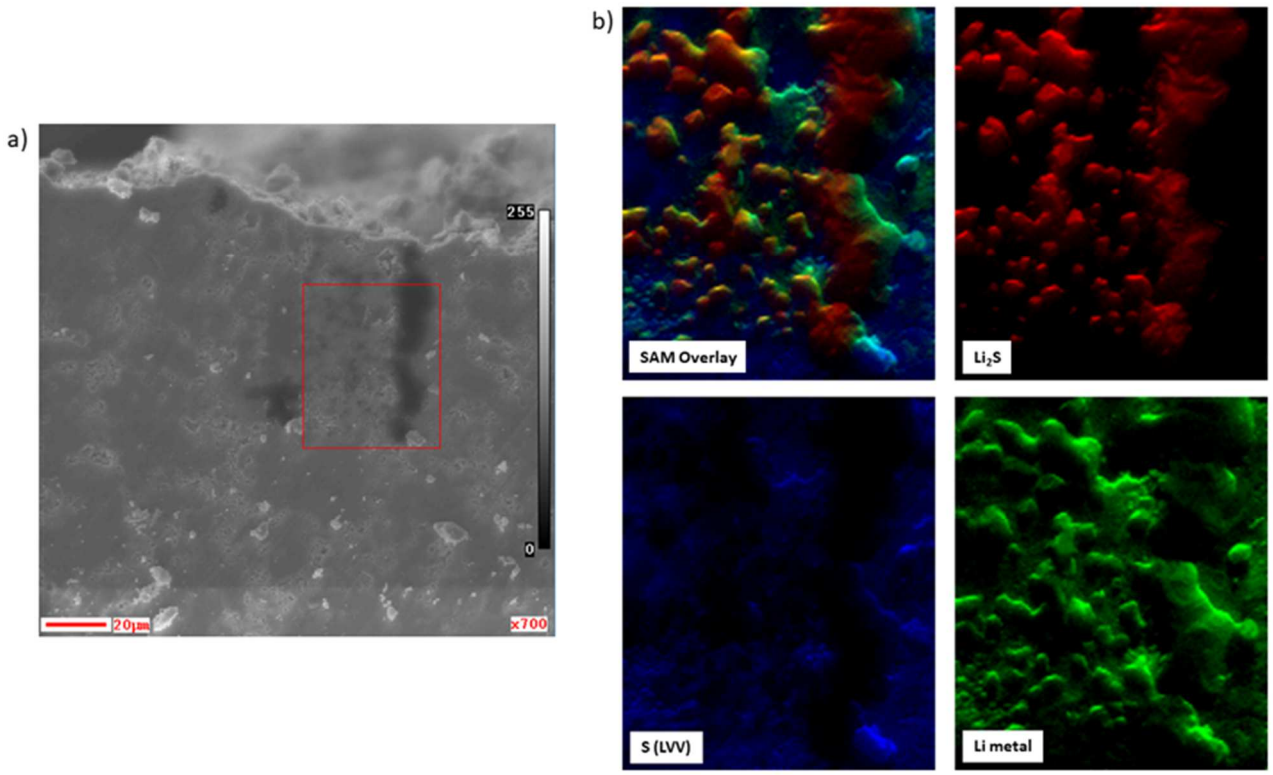

Fig. 4 a) SEM image of an Arg pellet surface in the middle of the operando Auger cycling using electrons beam with b) energy resolved SAM (elemental 2D distribution) images of Li_{metal} KVV, Li_{Li2S} KVV and S LVV transitions and their overlay.

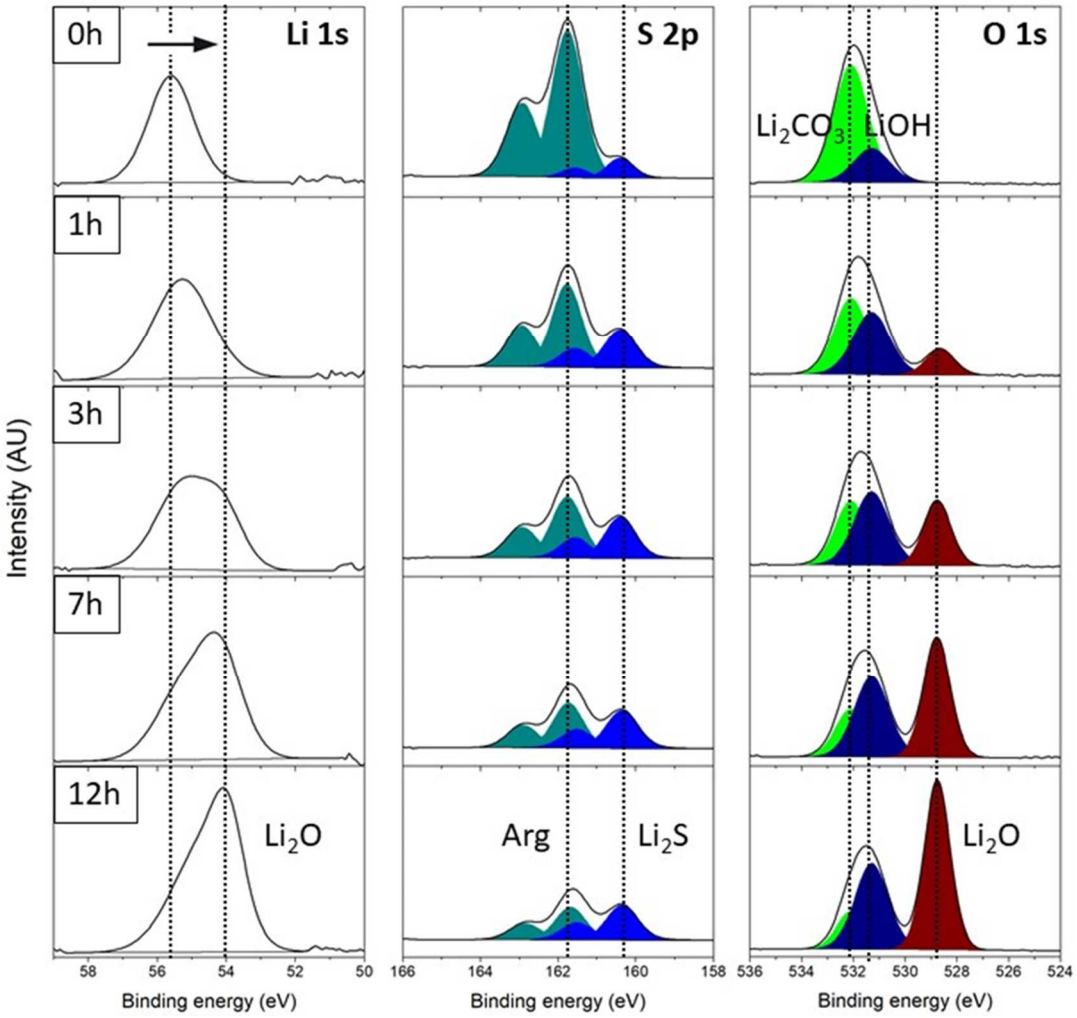

Fig. 5 XPS core level spectra of Li 1s, S 2p and O 1s as recorded at the Arg pellet surface during operando XPS cycling using electrons beam.

Table I. XPS quantification table (in at.%) of the main compounds and impurities as obtained from the XPS analysis of the Arg pellet surface during the *operando* XPS cycling using electrons beam.

Compounds	0h	1h	3h	7h	12h
Li_6PS_5Cl	37.2	21.6	14.4	10.8	7.2
Li_2S	5.1	10.8	10.8	9	7.8
LiCl	2.2	2.6	2.6	2.2	1.8
Li_2O	-	9.9	21.6	35.7	45.3
Li_xP	-	3.0	3.0	2.8	2.1
Li_2CO_3	24	16.8	13.8	10.8	7.8
P_2S_5	2.1	1.1	1.1	0.7	0.4
Li_xSO_3	7.5	3.5	3	1.5	1.5

Comparison between operando Auger and XPS – The combination of Auger and XPS allows validating the *operando* cycling method based on the use of an electron gun applied on a Li/Arg_{pellet} stack to evaluate the reduction pathway of Arg during Li plating. Interestingly, these spectroscopies bring complementary information. While *operando* XPS gave the evolution of the degradation species of the Arg solid electrolyte with reliable quantification, Auger allowed visualizing the dynamics of all the processes (volume expansion during Arg reduction, Li plating and its morphology) together with chemical information.

Beyond that, *operando* XPS showed the formation of LiOH then Li_2O instead of Li metal while *operando* Auger showed Li metal plating. Note that previous *operando* XPS studies already reported the formation of Li_2O instead of Li metal but did not discussed it[47,60,61]. At this point, both the analysis time and the analysis chamber pressure (*i.e.* residual O_2 pressure) can govern the Li_2O formation. In the present case, the duration of the *operando* Auger was 40 min while for *operando* XPS, it was 12 hour. Regarding the analysis chamber pressure, it was 1.5 x 10^{-9} mbar for Auger and almost one decade higher for XPS (9 x 10^{-9} mbar). To evaluate these parameters, the evolution of the Li metal plating (observed in Auger) was followed by recording additional SEM images and Auger spectra 20 min and 12h after the end of the *operando* Auger cycling procedure. At the end of the *operando* Auger, the SEM image showed the black contrast attributed to the Li metal plating with an additional white contrast on some areas (**Figure 6a**), attributed to Li_2O by comparison with JEOL references database (**Figure 6b**). After 20 more min or 12 h in the analysis chamber, the white areas significantly increased, indicating that Li metal continues to be converted into Li_2O (**Figure 6c and 6d**) but at a slow rate as Li metal is still observed (black areas). For comparison, Li metal was never observed by XPS. These results highlight that both the analysis time and chamber pressure govern the Li_2O formation, as expected. Therefore, *operando* Auger cycling and its fully tunable electron gun (both current and probe size) is of high interest to investigate both Li/solid electrolyte interphases formation and Li plating with its morphology as it could be done as function of the cycling rate. In *operando* XPS cycling, however, careful precaution should be taken if one want to strip the Li metal/Li_2O using the often available UV source as it could lead to misinterpretation of the results when only Li_2O is observed. In that case, in order to limit Li_2O formation, either the analysis time should be decrease by increasing the current and/or the chamber pressure should be lowered.

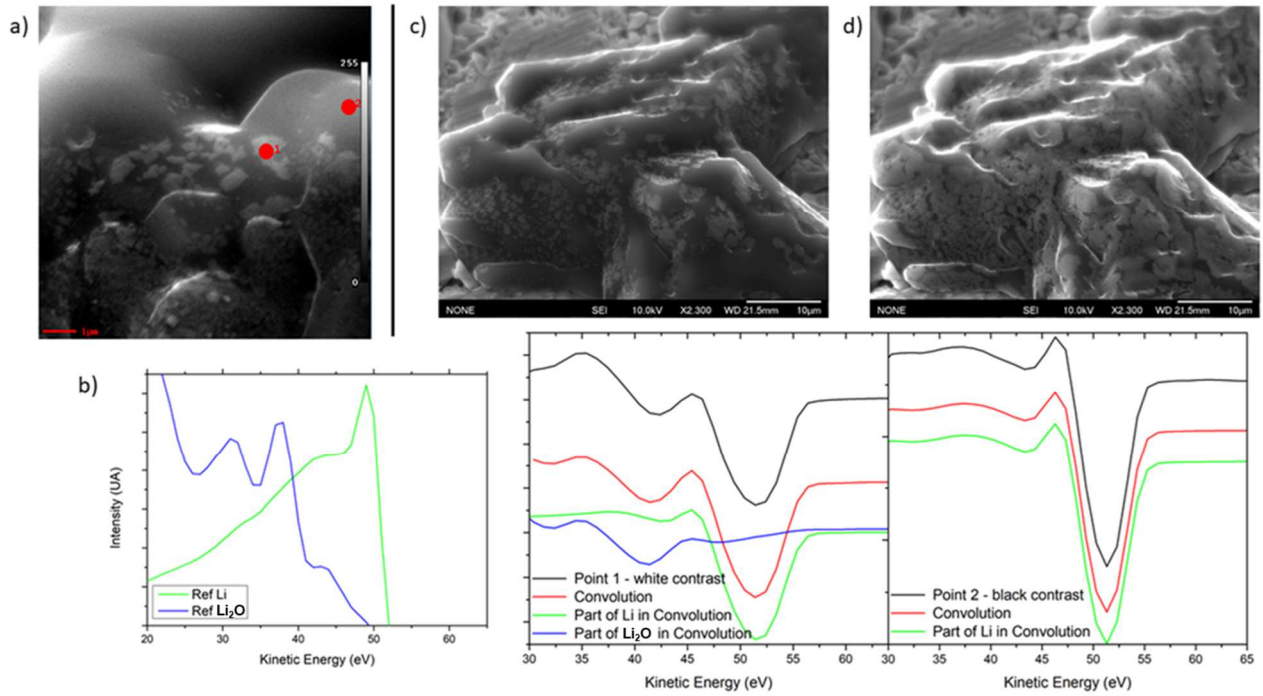

Fig. 6 SEM images as observed a) at the end of the operando Auger using electrons beam at the Arg pellet surface, c) 20 min later and d) 12 h later after the end of the operando Auger cycling procedure. b) Auger core level spectra of the Li KVV transition as recorded on two different points (black and white areas) as obtained at the end of the operando Auger, as indicated.

Conclusion

This work focuses on the use of *operando* Auger cycling to illustrate the high interest of this approach in the case of Li/solid electrolyte (SE) interphases study. This approach is based on the charges build up on top of an Li/SE stack using the fully tunable electron gun of Auger (current and probe size), which creates a potential difference then leads to the Li^+ migration from the lithium electrode and through the solid electrolyte, to SEI formation if any then to Li plating. Here, a model Li/Li_6PS_5Cl stack was used. Overall, it was showed that: (i) Arg is first reduced following the well-known $Li_6PS_5Cl + 8\ Li^+ + 8\ e^- \rightarrow LiCl + Li_3P + 5\ Li_2S$ pathway ; (ii) and Li plating occurs almost concomitantly ; (iii) then Li plating continues until the end of the *operando* cycling. These results were confirmed by *operando* XPS cycling on a pair Li/Li_6PS_5Cl stack. Interestingly, while *operando* XPS allows following the Li/SE interfaces formation with reliable quantification, Auger allows visualizing the dynamic of both interphase formation and Li plating with their morphologies together with chemical information. In the future, the fully tunable electron gun of Auger will be used to investigate both Li/SE interfaces formation and Li plating as function of the cycling rate as it is of high concerns in the literature. Overall, this work paves the way for future development of *operando* Auger cycling and for a better understanding of solid electrolyte reactivity (including halide, oxide etc. as well as polymer based electrolytes) in lithium solid-state batteries.

Author Contributions

We strongly encourage authors to include author contributions and recommend using CRediT for standardised contribution descriptions. Please refer to our general author guidelines for more information about authorship.

Conflicts of interest

“There are no conflicts to declare”.

Acknowledgements

This manuscript was produced as part of the RAISE2024 project. This project as received funding from the Excellence Initiative of Université de Pau et des Pays de l’Adour (I-Site E2S UPPA), a French “Investissement d’Avenir” program.

Notes and references

1 D. Andre, S. J. Kim, P. Lamp, S. F. Lux, F. Maglia, O. Paschos and B. Stiaszny, *J. Mater. Chem. A*, 2015, 3, 6709–6732.

2 A. Manthiram, X. Yu and S. Wang, *Nat. Rev. Mater.*, 2017, 2.

3 Q. Zhang, K. Liu, F. Ding and X. Liu, *Nano Res.*, 2017, 10, 4139–4174.

4 T. T. Zuo, R. Rueß, R. Pan, F. Walther, M. Rohnke, S. Hori, R. Kanno, D. Schröder and J. Janek, *Nat. Commun.*, , DOI:10.1038/s41467-021-26895-4.

5 I. López, J. Morey, J. B. Ledeuil, L. Madec and H. Martinez, *J. Mater. Chem. A*, 2021, **9**, 25341–25368.

6 W. Zaman and K. B. Hatzell, *Curr. Opin. Solid State Mater. Sci.*, 2022, **26**, 101003.

7 T. Abe, F. Sagane, M. Ohtsuka, Y. Iriyama and Z. Ogumi, *J. Electrochem. Soc.*, 2005, **152**, A2151.

8 S. S. Zhang, *ACS Appl. Energy Mater.*, 2018, **1**, 910–920.

9 T. Krauskopf, F. H. Richter, W. G. Zeier and J. Janek, *Chem. Rev.*, 2020, **120**, 7745–7794.

10 T. Krauskopf, H. Hartmann, W. G. Zeier and J. Janek, *ACS Appl. Mater. Interfaces*, 2019, **11**, 14463–14477.

11 Y. Zhu, X. He and Y. Mo, *ACS Appl. Mater. Interfaces*, 2015, **7**, 23685–23693.

12 M. Otoyama, H. Kowada, A. Sakuda, M. Tatsumisago and A. Hayashi, *J. Phys. Chem. Lett.*, 2020, **11**, 900–904.

13 S. Kim, C. Jung, H. Kim, K. E. Thomas-Alyea, G. Yoon, B. Kim, M. E. Badding, Z. Song, J. M. Chang, J. Kim, D. Im and K. Kang, *Adv. Energy Mater.*, 2020, **10**, 1–11.

14 M. Sun, T. Liu, Y. Yuan, M. Ling, N. Xu, Y. Liu, L. Yan, H. Li, C. Liu, Y. Lu, Y. Shi, Y. He, Y. Guo, X. Tao, C. Liang and J. Lu, *ACS Energy Lett.*, 2021, **6**, 451–458.

15 Y. X. Song, Y. Shi, J. Wan, S. Y. Lang, X. C. Hu, H. J. Yan, B. Liu, Y. G. Guo, R. Wen and L. J. Wan, *Energy Environ. Sci.*, 2019, **12**, 2496–2506.

16 W. Manalastas, J. Rikarte, R. J. Chater, R. Brugge, A. Aguadero, L. Buannic, A. Llordés, F. Aguesse and J. Kilner, *J. Power Sources*, 2019, **412**, 287–293.

17 E. Kazyak, R. Garcia-Mendez, W. S. LePage, A. Sharafi, A. L. Davis, A. J. Sanchez, K. H. Chen, C. Haslam, J. Sakamoto and N. P. Dasgupta, *Matter*, 2020, **2**, 1025–1048.

18 D. Santhanagopalan, D. Qian, T. McGilvray, Z. Wang, F. Wang, F. Camino, J. Graetz, N. Dudney and Y. S. Meng, *J. Phys. Chem. Lett.*, 2014, **5**, 298–303.

19 A. Aboulaich, R. Bouchet, G. Delaizir, V. Seznec, L. Tortet, M. Morcrette, P. Rozier, J. M. Tarascon, V. Viallet and M. Dollé, *Adv. Energy Mater.*, 2011, **1**, 179–183.

20 A. Brazier, L. Dupont, L. Dantras-Laffont, N. Kuwata, J. Kawamura and J. M. Tarascon, *Chem. Mater.*, 2008, **20**,

2352–2359.
21 J. Z. Lee, T. A. Wynn, Y. S. Meng and D. Santhanagopalan, *J. Vis. Exp.*, 2018, **2018**, 1–9.
22 A. Brazier, L. Dupont, L. Dantras-Laffont, N. Kuwata, J. Kawamura and J. M. Tarascon, *Chem. Mater.*, 2008, **20**, 2352–2359.
23 K. Yamamoto, R. Yoshida, T. Sato, H. Matsumoto, H. Kurobe, T. Hamanaka, T. Kato, Y. Iriyama and T. Hirayama, *J. Power Sources*, 2014, **266**, 414–421.
24 J. Auvergniot, A. Cassel, D. Foix, V. Viallet, V. Seznec and R. Dedryvère, *Solid State Ionics*, 2017, **300**, 78–85.
25 A. Uhart, J. B. Ledeuil, B. Pecquenard, F. Le Cras, M. Proust and H. Martinez, *ACS Appl. Mater. Interfaces*, 2017, **9**, 33238–33249.
26 M. Yamamoto, Y. Terauchi, A. Sakuda, A. Kato and M. Takahashi, *J. Power Sources*, 2020, **473**, 228595.
27 J. Zagórski, B. Silván, D. Saurel, F. Aguesse and A. Llordés, *ACS Appl. Energy Mater.*, 2020, **3**, 8344–8355.
28 D. Cheng, T. A. Wynn, X. Wang, S. Wang, M. Zhang, R. Shimizu, S. Bai, H. Nguyen, C. Fang, M. cheol Kim, W. Li, B. Lu, S. J. Kim and Y. S. Meng, *Joule*, 2020, **4**, 2484–2500.
29 X. Li, Z. Ren, M. Norouzi Banis, S. Deng, Y. Zhao, Q. Sun, C. Wang, X. Yang, W. Li, J. Liang, X. Li, Y. Sun, K. Adair, R. Li, Y. Hu, T. K. Sham, H. Huang, L. Zhang, S. Lu, J. Luo and X. Sun, *ACS Energy Lett.*, 2019, **4**, 2480–2488.
30 J. B. Ledeuil, A. Uhart, S. Soulé, J. Allouche, J. C. Dupin and H. Martinez, *Nanoscale*, 2014, **6**, 11130–11140.
31 M. Otoyama, Y. Ito, A. Hayashi and M. Tatsumisago, *J. Power Sources*, 2016, **302**, 419–425.
32 F. Walther, R. Koerver, T. Fuchs, S. Ohno, J. Sann, M. Rohnke, W. G. Zeier and J. Janek, *Chem. Mater.*, , DOI:10.1021/acs.chemmater.9b00770.
33 F. Walther, S. Randau, Y. Schneider, J. Sann, M. Rohnke, F. H. Richter, W. G. Zeier and J. Janek, *Chem. Mater.*, 2020, **32**, 6123–6136.
34 F. Walther, F. Strauss, X. Wu, B. Mogwitz, J. Hertle, J. Sann, M. Rohnke, T. Brezesinski and J. Janek, *Chem. Mater.*, 2021, **33**, 2110–2125.
35 N. Wu, P. H. Chien, Y. Li, A. Dolocan, H. Xu, B. Xu, N. S. Grundish, H. Jin, Y. Y. Hu and J. B. Goodenough, *J. Am. Chem. Soc.*, 2020, **142**, 2497–2505.
36 J. Liang, S. Hwang, S. Li, J. Luo, Y. Sun, Y. Zhao, Q. Sun, W. Li, M. Li, M. N. Banis, X. Li, R. Li, L. Zhang, S. Zhao, S. Lu, H. Huang, D. Su and X. Sun, *Nano Energy*, 2020, **78**, 105107.
37 R. Schlenker, D. Stępień, P. Koch, T. Hupfer, S. Indris, B. Roling, V. Miß, A. Fuchs, M. Wilhelmi and H. Ehrenberg, *ACS Appl. Mater. Interfaces*, 2020, **12**, 20012–20025.
38 C. Xu, B. Sun, T. Gustafsson, K. Edström, D. Brandell and M. Hahlin, *J. Mater. Chem. A*, 2014, **2**, 7256–7264.
39 J. Auvergniot, A. Cassel, J. B. Ledeuil, V. Viallet, V. Seznec and R. Dedryvère, *Chem. Mater.*, 2017, **29**, 3883–3890.
40 B. Sun, C. Xu, J. Mindemark, T. Gustafsson, K. Edström and D. Brandell, *J. Mater. Chem. A*, 2015, **3**, 13994–14000.
41 S. A. Pervez, B. P. Vinayan, M. A. Cambaz, G. Melinte, T. Diemant, T. Braun, G. Karkera, R. J. Behm and M. Fichtner, *J. Mater. Chem. A*, 2020, **8**, 16451–16462.
42 J. Qiu, X. Liu, R. Chen, Q. Li, Y. Wang, P. Chen, L. Gan, S. J. Lee, D. Nordlund, Y. Liu, X. Yu, X. Bai, H. Li and L. Chen, *Adv. Funct. Mater.*, 2020, **30**, 1–8.
43 S. Larfaillou, D. Guy-Bouyssou, F. Le Cras and S. Franger, *ECS Trans.*, 2014, **61**, 165–171.
44 N. Grillon, E. Bouyssou, S. Jacques and G. Gautier, *J. Electrochem. Soc.*, 2015, **162**, A2847–A2853.
45 S. Larfaillou, D. Guy-Bouyssou, F. Le Cras and S. Franger, *J. Power Sources*, 2016, **319**, 139–146.
46 F. Strauss, D. Kitsche, Y. Ma, J. H. Teo, D. Goonetilleke, J. Janek, M. Bianchini and T. Brezesinski, *Adv. Energy Sustain. Res.*, 2021, **2**, 2100004.
47 A. L. Davis, E. Kazyak, J. Sakamoto, N. P. Dasgupta, R. Garcia-Mendez, K. H. Chen, J. Sakamoto, K. N. Wood, G. Teeter and K. N. Wood, *J. Mater. Chem. A*, 2020, **8**, 6291–6302.
48 M. Golozar, A. Paolella, H. Demers, S. Savoie, G. Girard, N. Delaporte, R. Gauvin, A. Guerfi, H. Lorrmann and K. Zaghib, *Sci. Rep.*, 2020, **10**, 1–11.
49 K. N. Wood, K. X. Steirer, S. E. Hafner, C. Ban, S. Santhanagopalan, S. H. Lee and G. Teeter, *Nat. Commun.*, 2018, **9**, 1–10.
50 Y. K. Sun and P. V. Kamat, *ACS Energy Lett.*, 2021, **6**, 2356–2358.
51 L. Yang, W. You, X. Zhao, H. Guo, X. Li, J. Zhang, Y. Wang and R. Che, *Nanoscale*, 2019, **11**, 17557–17562.
52 X. Liu, D. Wang, G. Liu, V. Srinivasan, Z. Liu, Z. Hussain and W. Yang, *Nat. Commun.*, 2013, **4**, 1–8.
53 J. M. Lee, Y. S. Park, J. W. Moon and H. Hwang, *Front. Chem.*, 2021, **9**, 1–8.
54 AMPCERA Argyrdite Li6PS5CL Sulfide Solid Electrolyte, Pass 150 Mesh (Below 100µm) Coarse Powder, https://www.msesupplies.com/collections/electrolyte-materials/products/ampcera-sulfide-solid-electrolyte-argyrodite-li6ps5cl-powder?variant=22924472614970.
55 Y. Zhou, C. Doerrer, J. Kasemchainan, P. G. Bruce, M. Pasta and L. J. Hardwick, *Batter. Supercaps*, 2020, **3**, 647–652.
56 D. H. S. Tan, E. A. Wu, H. Nguyen, Z. Chen, M. A. T. Marple, J. M. Doux, X. Wang, H. Yang, A. Banerjee and Y. S. Meng, *ACS Energy Lett.*, 2019, 2418–2427.
57 S. Wenzel, T. Leichtweiss, D. Krüger, J. Sann and J. Janek, *Solid State Ionics*, 2015, **278**, 98–105.
58 S. Wenzel, S. J. Sedlmaier, C. Dietrich, W. G. Zeier and J. Janek, *Solid State Ionics*, 2018, **318**, 102–112.
59 Y. Zhu, X. He and Y. Mo, *ACS Appl. Mater. Interfaces*, 2015, **7**, 23685–23693.
60 M. I. Nandasiri, L. E. Camacho-Forero, A. M. Schwarz, V. Shutthanandan, S. Thevuthasan, P. B. Balbuena, K. T. Mueller and V. Murugesan, *Chem. Mater.*, 2017, **29**, 4728–4737.
61 M. Mirolo, X. Wu, C. A. F. Vaz, P. Novák and M. El Kazzi, *ACS Appl. Mater. Interfaces*, 2021, **13**, 2547–2557.

